Highly efficient plasmon-mediated electron injection into cerium oxide from embedded silver nanoparticles / Pelli Cresi, J. S.; Spadaro, M. C.; D'Addato, S.; Valeri, S.; Benedetti, S.; Di Bona, A.; Catone, D.; Di Mario, L.; O'Keeffe, P.; Paladini, A.; Bertoni, G.; Luches, P.. - In: NANOSCALE. - ISSN 2040-3364. - 11:21(2019), pp. 10282-10291. [10.1039/c9nr01390c]

ARTICLE

Highly efficient plasmon-mediated electron injection into cerium oxide from embedded silver nanoparticles

Received 00th January 20xx,
Accepted 00th January 20xx

DOI: 10.1039/x0xx00000x

Jacopo Stefano Pelli Cresi [a,b], Maria Chiara Spadaro [a,b], Sergio D`Addato [a,b], Sergio Valeri [a,b], Stefania Benedetti[a,b], Alessandro Di Bona[b], Daniele Catone[c], Lorenzo Di Mario[c], Patrick O'Keeffe [d], Alessandra Paladini [d], Giovanni Bertoni [e], Paola Luches [b*]

The coupling with plasmonic metal nanoparticles (NPs) represents a promising opportunity to sensitize wide band gap oxides to visible light. The processes which come into play after the excitation of localized surface plasmon resonances (LSPR) in the NPs largely determine the efficiency of the charge/energy transfer from the metal NP to the oxide. We report a study of plasmon mediated energy transfer from mass-selected silver NPs into the cerium oxide matrix in which they are embedded. Femtosecond transient absorption spectroscopy is used to probe the dynamics of charge carrier relaxation after the excitation of the LSPR of the silver nanoparticles and to evaluate the plasmon-mediated electron transfer efficiency from the silver nanoparticles to the cerium oxide. High injection efficiencies in the 6-16 % range have been identified for excitation between 400 and 600 nm. These high values have been explained in terms of plasmon-mediated direct electron injection as well as indirect hot electron injection from the NPs to the oxide. The information obtained provide an important contribution towards a knowledge-driven design of efficient cerium oxide based nanostructured materials for solar to chemical energy conversion.

Introduction

The study of plasmon-mediated photocatalysis has increased very rapidly in recent years due to the possibility of extending the energy range of activity of traditional semiconductor photocatalysts, as in the case of the water splitting reaction induced by TiO_2 sensitized by gold nanoparticles (NPs).[1–7] This is generally achieved by taking advantage of the large cross section for the absorption and scattering of visible light of plasmonic metal nanostructures placed in the vicinity of a semiconductor substrate, thus creating a metal/semiconductor interface across which electrons can be transferred.[8–10] In the class of semiconductor catalysts, cerium oxide CeO_2 (the material studied here) is attracting a growing interest due to its efficiency in catalyzing redox reactions.[11–14] In CeO_2 the presence of localized Ce 4f states between the O 2p valence band and the Ce 5d conduction band makes the material a very sensitive probe to identify charge transfer to/from neighboring metal atoms.[15] The occupation of 4f levels is in turn expected to modify the material properties, inducing a decrease of oxygen vacancy formation energy, and a change of the optical response.[16,17]

A plethora of different mechanisms for the transfer of energy from metal NPs to semiconductors have been identified and recently reviewed.[18–21] The dominant processes which come into play are: i) the enhancement of an optical transition within the semiconductor due to the presence of the plasmonic NPs,[6] ii) hot electron injection from the plasmonic NPs to the semiconductor,[6] and the recently described iii) direct metal-to-semiconductor interfacial charge transfer. [22,23]

The first of these is actually a group of mechanisms, which require an overlap between the localized surface plasmon resonance (LSPR) of the NPs and the absorption band of the semiconductor and rely on the high light absorption cross section of the nanostructures to efficiently convert the energy of the light into electronic transitions within the semiconductor. These mechanisms include light trapping, by which we mean multiple and high angle elastic scattering of light by the NPs, leading to an increase in the effective optical path,[18] energy transfer to the semiconductor through near-field enhancement in the vicinity of the NPs, [19] plasmon-induced radiative energy transfer in which photons emitted by the NPs are absorbed by the semiconductor,[19] and plasmon-induced resonant energy transfer.[24] In general, these processes contribute little to the efficiency of visible light energy transfer in the case of wide band gap semiconductors, which have low absorption cross sections in this region (e.g. TiO_2). The second mechanism involves the formation of hot electrons in the metallic NPs either by interband transitions or decay of the LSPR by Landau

ha eliminato: The main text of the article should appear here with headings as appropriate.

ha eliminato: the

---

[a] *Dipartimento FIM, Università di Modena e Reggio Emilia, Via G. Campi 213/a, Modena, Italy*
[b] *CNR-NANO, Centro di Ricerca S3, via G. Campi 213/a, Modena, Italy*
[c] *CNR-ISM, Division of Ultrafast Processes in Materials (FLASHit), Area della Ricerca di Roma Tor Vergata, Via del Fosso del Cavaliere, 100, Rome, Italy*
[d] *CNR-ISM, Division of Ultrafast Processes in Materials (FLASHit), Area della Ricerca di Roma 1, Monterotondo Scalo, Italy*
Istituto dei Materiali per l'Elettronica ed il Magnetismo, Consiglio Nazionale delle Ricerche, Parco Area delle Scienze 37/A, I-43124, Parma, Italy
** Corresponding Author e-mail: paola.luches@nano.cnr.it*

Electronic Supplementary Information (ESI) available: [details of any supplementary information available should be included here]. See DOI: 10.1039/x0xx00000x

damping. The hot electrons can be transferred over/through the Schottky barrier formed at the interface into empty levels of the semiconductor. Finally, a mechanism has been proposed involving direct electron transfer during the excitation light pulse: the decay of the LSPR directly excites electrons into acceptor states of the semiconductor and leaves holes in the metal.[22,23] This process is possibly more efficient than the indirect transfer, where the hot electrons generated in the metal NP can be partially quenched by electron-electron and electron-phonon scattering before the injection.[6]

The relative contributions of the different mechanisms depend on numerous factors such as the shape, the density and the composition of the NPs, the band structure of the semiconductor, the morphology of the interface and many more. For example, an important factor to consider is the near-field concentration of light due to the nanoantenna effect of the metallic nanostructures.[25] It is well known that the spatial distribution of the electromagnetic field intensity is strongly dependent on the NPs shape and size and that it can be highly concentrated in specific sites, in particular in the case of interacting NPs with small interparticle distance or sharp edges. In the hot spots formed in this way the efficiency of the electron injection mechanism can be significantly modified.[25–29] Moreover, it was shown that by embedding the metallic nanostructures into the semiconductor it is possible to significantly increase the injection efficiency due to a more extended metal-semiconductor contact area.[30,31]

In this work we use femtosecond transient absorption spectroscopy (FTAS) to investigate the mechanisms of LSPR decay in silver NPs embedded in a thin film of CeO_2. The samples are accurately controlled in stoichiometry and morphology, based on our previous experience with cerium oxide films in combination with Ag NPs.[16,32] To maximize the Ag/CeO_2 interface and to prevent Ag oxidation the NPs are embedded within a cerium oxide matrix (Ag@CeO_2). We obtained very high electron injection efficiencies (6-16 %) that we discuss in terms of the above mechanisms, analyzing the role of the morphology of the metal NPs, of the metal/semiconductor interface, as well as the near-field light concentration effects due to hot-spot generation by the metal NPs.

Methods

The NPs were synthesized using a magnetron sputtering nanocluster source by inert gas aggregation (NC200U, Oxford Applied Research). The source chamber is part of an ultrahigh vacuum system that includes also an X-ray photoelectron spectroscopy (XPS) apparatus (a double anode x-ray source – Specs XR50 coupled with a hemispherical electron analyzer - Specs Phoibos 150) for in-situ chemical characterization. Silver NPs were obtained from a 99.9% pure Ag target (P_{shot}=68 W) with an Ar gas flow (f_{Ag} = 59 sccm) in the aggregation region and they were mass selected using a quadrupole mass filter (QMF200, Oxford Applied Research), set to select NPs with a mass of 10^6 amu (F=5 kHz, V=250 V). The deposition chamber was equipped with an electron bombardment evaporation cell, which was used to evaporate cerium oxide films using an oxygen partial pressure of P_{O2}=5 x 10^{-6} mbar. The chamber hosted a quartz crystal microbalance, which was used to estimate the evaporation rates from the nanocluster source and from the cerium evaporator before the growth. The sample under study was grown on a quartz substrate (fused silica EQX thickness 1 mm) kept at room temperature by the sequential deposition of a cerium oxide film of 5 nm thickness, a layer of Ag NPs of 5 nm nominal thickness and a cerium oxide film of 5 nm thickness. The nominal thickness of the NP layer is defined as the thickness of a homogeneous film with the same volume as the NP layer. The two cerium oxide films were exposed to an oxygen partial pressure P_{O2} = 6 x 10^{-5} mbar for 30 min after the growth, to maximize the Ce^{4+} concentration. After each growth step the sample was characterized in-situ by XPS using Al-K_α photons to obtain quantitative information on the amount of CeO_2 and Ag deposited and on the oxidation state of CeO_2 (see Supporting Information, Figure S4). In addition to the Ag@CeO_2 sample, we investigated also a reference sample, which consists of a 10 nm cerium oxide film without Ag NPs on a quartz substrate.

To investigate shape, size distribution and crystal quality of Ag NPs, ex-situ scanning transmission electron microscopy (STEM) in annular dark field mode and high-resolution transmission electron microscopy (HRTEM) measurements were performed using a JEOL JEM-2200FS microscope (IMEM-CNR, Parma) equipped with a Schottky emitter working at 200 keV (point resolution 0.19 nm). All of the images were analyzed using ImageJ software.[33] The sample used for TEM measurements was grown by co-evaporating 0.05 ML of Ag NPs and 2 nm of CeO_2 on a carbon-coated copper grid. The nanocluster source conditions were the same used to grow the sample for the optical characterization, except for the lower density of Ag NPs, chosen in order to distinguish individual NP and to allow for a more detailed characterization.

Steady UV-Vis spectrophotometry measurements were performed using a white non-polarized light source generated by a Xenon lamp, equipped with an ORIEL-MS257 monochromator and a silicon photodetector (with a 250-750 nm range of detection). The samples were oriented so that the sample surface normal formed an incident angle of 22° with the incident photon beam. We evaluated the absorbance A by measuring the fraction of transmitted T and specular reflected R light (A=1-T-R).

The MNPBEM toolbox developed by Hohenester and coworkers,[34] based on the boundary element method (BEM) approach developed by García de Abajo et al.[35] was used to calculate the absorption, scattering and extinction coefficients of metal NPs embedded in and sitting on CeO_2. The dielectric constants for CeO_2 and Ag were taken from ref. [36] and [37], respectively.

The ultrafast carrier dynamics of our samples were studied by FTAS using a pump-probe femtosecond laser system consisting of a chirped pulse amplifier seeded by a Ti:Sa oscillator (800 nm, 1 KHz, 4 mJ, 35 fs).[38] The pump pulses were generated by an optical parametric amplifier (OPA), pumped by the amplifier. The probe for the TA measurements is a white light

ha eliminato: also
ha eliminato: of
ha eliminato: of
ha eliminato: deposited
ha eliminato: but a smaller
ha eliminato: t
ha eliminato: was
ha eliminato: i
ha eliminato: s
ha eliminato: obtain
ha eliminato: forms
ha eliminato: Dielectric
ha eliminato: are
ha eliminato: also

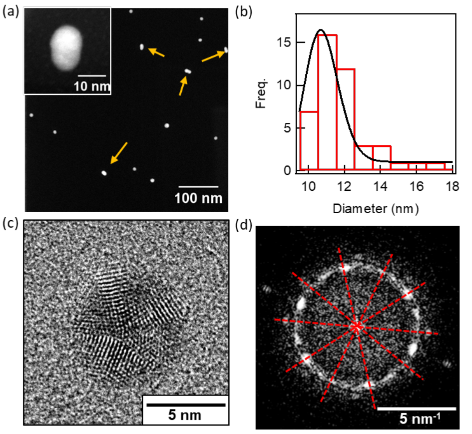

Figure 1. TEM images of Ag@CeO$_2$: a) large scale STEM image, the detail of a NP formed by the coalescence of two single NPs is shown in the inset; b) size distribution evaluated from a series of STEM images and fit by a lognormal curve; c) HRTEM of a single NP; d) Fourier transform of the image in c).

supercontinuum generated in a Fast Transient Spectrometer of IB Photonics (FemtoFrame II). The probe wavelengths ranged between 260 and 760 nm, while the pump-probe delay time was scanned up to 500 ps. The probe energy range was covered focusing the fundamental (800 nm) or the second harmonic (400 nm) radiation of the amplifier into a rotating CaF$_2$ window that generates the white light supercontinuum in the 320-780 nm (visible probe) and 260-380 nm (UV probe) energy ranges, respectively. The IRF was measured to be approximately 50 fs. This setup allowed both the energy regions of the LSPR of Ag NPs and the cerium oxide band gap to be probed. The study of electron injection efficiency was performed using different pump fluences ranging from 45 to 900 μJ/cm^2.

Results and discussion

The plasmonic properties of metal NPs are strongly dependent on their size and shape. For this reason, a detailed characterization of the sample morphology is mandatory to understand the origin of the optical absorption features. We therefore investigated an Ag@CeO$_2$ sample made of NPs with the same size and a lower density, compared to the one used for the optical studies, to be able to analyze individual NPs by TEM/STEM (see Methods). Figure 1a shows a representative STEM image of a portion of the sample. The NP size distribution shown in Figure 1b, was obtained by considering the minimum Feret diameter, evaluated using ImageJ software[33], on a series of images. The size distribution has a maximum around 10.5 nm and a FWHM of 2.4 nm. HRTEM was used to obtain detailed information on the NPs shape and crystallinity. Most of the individual NPs have a polyhedral shape and a multi-twinned structure (see Supporting Information for details). As an example we show the HRTEM image of a NP with a five-fold symmetry (Figure 1c), possibly originating from a decahedral shape (see Supporting Information) and the corresponding Fourier transform with a ten-fold symmetry (Figure 1d). As observed in previous works, these phases are thermodynamically metastable and they can be stabilized by fast quenching rates for fcc metal NPs. [39,40] The image in Figure 1c shows a well-defined crystal structure only in some portions of the NP, while other areas show a more uniform contrast, which indicates a lower degree of crystalline order. Figure 1a also shows a non-negligible presence of agglomerates of two or three merged NPs (yellow arrows), one of which is reported in detail in the inset. Some degree of coalescence of NPs grown by the physical method used here has already been reported [41] and it was ascribed to a non-negligible probability for the NPs to merge either in-flight or on the substrate after the deposition. The granular features evident on the dark area in the inset of Figure 1a are ascribed to the presence of a cerium oxide layer covering the substrate and the NPs, as confirmed also by energy dispersive X-ray analysis (data not shown).

Figure 2. Absorbance spectra **of quartz (red line), CeO$_2$ film (blue line) and Ag@CeO$_2$ sample (green line).** shows the static UV-Vis absorbance spectra of the quartz substrate (red line),, of the CeO$_2$ thin film (blue line) and of the Ag@CeO$_2$ sample (green line). Here we define absorbance by the formula A=1-T-R where T is the transmittance and R is the specular reflectance (the UV-Vis transmittance and reflectance spectra are reported in the Supporting Information as Figure S2). As expected, the quartz substrate does not show significant absorption in the UV-Vis range, while the CeO$_2$ thin film shows strong absorption at wavelengths below 350 nm, where the band edge absorption sets in. The extraction of the optical band gap from a Tauc plot of $(\alpha h\nu)^{1/2}$ vs. hν yields a value of 3.44 ± 0.03 eV (see Supporting Information, Figure S3) that is in good agreement with the range of values 3.0 - 3.6 eV obtained for ceria films prepared by sputter deposition or thermal evaporation.[42,43] In general, a red shift of the optical band gap from the pure bulk value is indicative of the presence of Ce^{3+} and oxygen defects.[44–46] Nonetheless, the CeO$_2$ film used here is of good quality, as when defects are intentionally added much larger optical shifts are observed.[47] The analysis of the Ce 3d XPS lineshape (see Supporting Information, Figure S4) demonstrates a stoichiometry close to CeO$_2$ for the ceria layer. The presence of a small absorbance in the visible region (approx. 5 %) in the CeO$_2$ film spectrum can be assigned to the roughness of the thin film, which gives rise to some diffuse reflectance and consequently to a non-negligible apparent absorbance. The

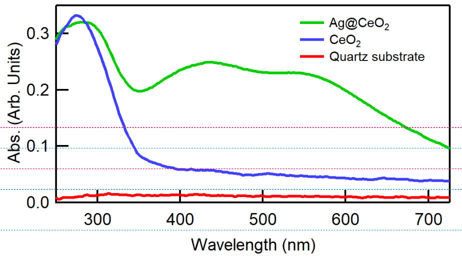

Figure 2. Absorbance spectra of quartz (red line), CeO$_2$ film (blue line) and Ag@CeO$_2$ sample (green line).

ha formattato: Tipo di carattere: Non Grassetto, Proporzioni car 108%

ha eliminato: Figure 1Figure 1

ha formattato: Tipo di carattere: Non Grassetto, Proporzioni car 108%

ha eliminato: (see Figure S1, Supporting Information)

ha formattato: Tipo di carattere: Non Grassetto, Proporzioni car 108%

ha eliminato: Figure 1Figure 1

ha formattato: Tipo di carattere: Non Grassetto, Proporzioni car 108%

ha eliminato: Figure 1d

ha eliminato: figure

ha eliminato: d

ha formattato: Tipo di carattere: Non Grassetto, Proporzioni car 108%

ha formattato: Tipo di carattere: Non Grassetto, Proporzioni car 108%

ha eliminato: Figure 2. Figure 2

ha formattato: Tipo di carattere: Non Grassetto, Proporzioni car 108%

ha formattato: Tipo di carattere: Non Grassetto

ha eliminato: ;

ha eliminato: detail of a NP formed by the coalescence of two single NPs.

ha eliminato: .

ha eliminato: a

ha eliminato: a

ha eliminato: E

ha eliminato: of

ha formattato: Tipo di carattere: Non Grassetto, Proporzioni car 108%

ha eliminato: Figure 1Figure 1

ha formattato: Tipo di carattere: Non Grassetto, Proporzioni car 108%

ha eliminato: , used to evaluate t

ha formattato: Tipo di carattere: Non Grassetto, Proporzioni car 108%

ha eliminato: Figure 1Figure 1

ha formattato: Tipo di carattere: Non Grassetto, Proporzioni car 108%

ha formattato: Apice

ha formattato: Non Apice / Pedice

ha eliminato: (Figure 1c)

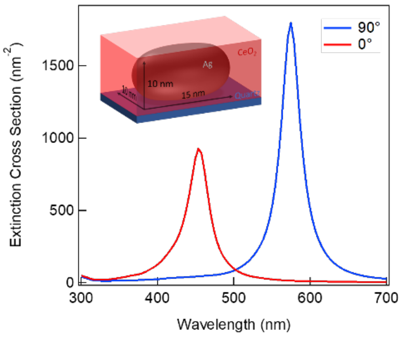

Figure 4 Simulated extinction cross section spectra obtained using the MNPBEM toolbox [34] with a linearly polarized light parallel (red curves) and perpendicular (blue curves) to the minor axis of embedded ellipsoidal NPs with geometry 15 × 10 × 10 nm^3 embedded in a 10 nm thick ceria film.

incorporation of Ag NPs into the CeO$_2$ film significantly modifies the absorbance spectrum with the appearance of two broad peaks with maxima at 420 and 580 nm, assigned to the LSPR in Ag NPs, shifted into the visible range due to the high dielectric constant of CeO$_2$. The presence of two peaks can be either due to an anisotropic NPs shape, giving rise to transverse and longitudinal LSPRs at different wavelengths, or to the superposition of LSPRs and delocalized plasmon resonances involving closely spaced interacting spherical NPs. We have ruled out the second possibility because the average distance between the Ag NPs in our samples, estimated using the measured deposited amount of NPs (see Methods) and their average size, is too large to induce an extended plasmon resonance (see Supporting Information, Figure S5).[48,49] The STEM images in Figure 1 show the presence of a fraction of anisotropically shaped NPs formed by the coalescence of individual Ag NPs during the deposition process. We tentatively ascribe the presence of two peaks in the Ag@CeO$_2$ absorbance spectra to the NP anisotropy.

The MNPBEM toolbox developed by Hohenester and coworkers,[34] was used to confirm the origin of the two LSPR peaks by simulating the absorption spectrum of the Ag@CeO$_2$ sample. The shape of the NPs observed by TEM/STEM was approximated using different geometries, including nanorods, spheroids, ellipsoids and nanodisks (see Supporting Information, Figure S5). The best agreement with the experimental data was obtained using ellipsoidal NPs with 10 and 15 nm in-plane axes and 10 nm out-of-plane axis, embedded within a 10 nm thick CeO$_2$ film. This geometry is compatible with the measured average size and shape of the NPs and with the thickness of the oxide matrix of the sample investigated here. The calculated extinction cross section spectra for this configuration, reported in Figure 3, show two peaks at 450 nm and 590 nm with the light polarization respectively parallel and perpendicular to the minor axis of the ellipsoid. Based on the results of the simulations, the two broad peaks with maxima at 450 and 580 nm in the experimental spectra acquired using non-polarized light can be assigned to the excitation of the two LSPRs in the anisotropic Ag NPs embedded within the cerium oxide matrix. The large width and different relative intensity of the peaks observed in the experimental spectra are ascribed to the aspect ratio distribution of the NPs. Figure 4b shows the false-color map of transient absorbance (TA) spectra of the CeO$_2$ film without Ag NPs, excited with a pump at 275 nm (4.5 eV), significantly above the optical band gap of the CeO$_2$ film. The map has been constructed by combining the maps recorded using the UV (285-350 nm) and visible (340-750 nm) white light supercontinuum probes. It reports the TA intensity as a function of the probe wavelength (y-axis) and of the time delay between pump and probe (x-axis), and it provides information about the dynamics of the photoexcited states in the CeO$_2$ sample. The TA map is dominated by two main features: a negative peak at 300 nm and a positive peak around 350 nm. The two features show only a slight decrease in intensity with increasing delay time up to 500 ps, which suggests that the corresponding excited electrons are stable to recombination, possibly due to trapping in localized states.[50] The negative peak corresponds to the wavelength of the maximum of the absorbance spectrum of CeO$_2$ (Figure 2) and it is ascribed to photoinduced bleaching (PB) of the O 2p band. Considering the band structure of CeO$_2$ with a valence band of O 2p character, a conduction band of Ce 5d character and Ce 4f levels in between (Figure 4a), we assign the positive peak at 345 nm (3.3 eV) to photoinduced absorption of electrons excited by the pump from the valence band to Ce 4f levels and further excited into the Ce 5d band by the probe. This assignment is supported also by the smaller energy separation between the 4f and 5d bands ($E_{4f\text{-}5d}$ ~ 3 eV) in stoichiometric CeO$_2$, [51,52] compared to the energy separation between filled O 2p and empty Ce 4f ($E_{2p\text{-}4f}$ ~ 3.3 eV [51,52]) states, compatible with the higher energy of the ground state bleaching compared to

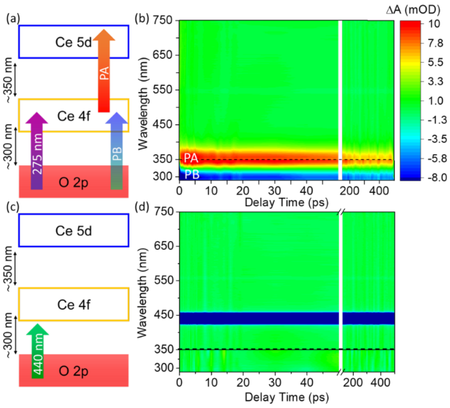

Figure 3. Sketch of the cerium oxide electronic structure, showing (a) the transitions induced by the pump at 275 nm and the corresponding TA signals and (c) the absence of transitions with the pump at 440 nm. False-color map of the TA spectra for the CeO$_2$ sample excited with a pump at 275 nm (b) and at 440 nm (d) and probed with both UV and visible white light supercontinuum probes at different delay times (from 3 to 500 ps); the black dashed line at 350 nm separates the two sets of data acquired with the two different probes. The blue intense line centered at 440 nm is the scattered light from the pump.

ha eliminato: is

ha eliminato: ¶

ha eliminato: Figure 4Figure 4

ha eliminato:

ha eliminato: 3

ha eliminato: Figure 4b

ha eliminato: Figure 4Figure 4

ha eliminato: absorption

ha eliminato: ,

ha eliminato: well

ha eliminato: 4

ha eliminato: a) False-color map of the TA spectra for the CeO$_2$ sample excited with a pump at 275 nm and probed with both UV and visible white light supercontinuum probes at different delay times (from 3 to 500 ps); the black dashed line at 350 nm separates the two sets of data acquired with the two different probes. b)

ha eliminato: here

ha eliminato: b

ha eliminato: .

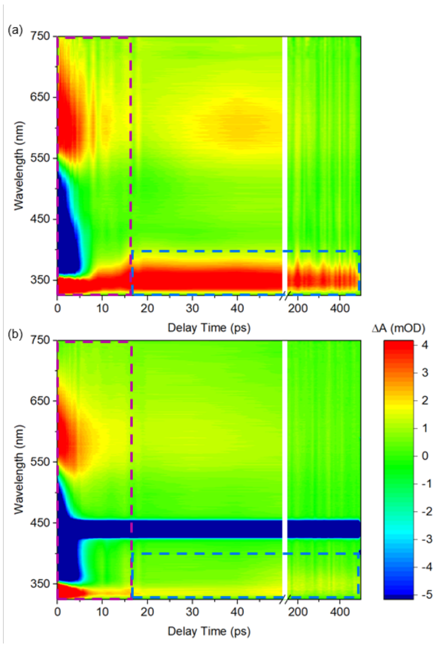

Figure 5. False-color maps of the TA spectra obtained for the Ag@CeO$_2$ sample excited with a pump (a) at275 nm, i.e. above the CeO$_2$ band gap, and (b) at 440 nm, i.e. below the CeO$_2$ band gap at LSPR maximum. The red box highlights the part of the map dominated by the plasmonic response of the Ag NPs while the blue box contains the signals assigned to electron injection into the CeO$_2$ film. The blue intense line centered at 440 nm is the scattered light from the pump.

the photoinduced absorption features in the TA spectra reported in Figure 4b. Indeed, the density of states in the valence band slightly depends on the average oxidation state of cerium ions and on the density and kind of defects. Figure 4d reports the TA map acquired on the same CeO$_2$ sample, using a pump below the band gap threshold (440 nm). The absence of TA features is in agreement with the assignment made for the features in the TA map in Figure 4a. The negative intensity in the 425-455 nm wavelength range is due to scattering of the photons with a 440 ± 15 nm wavelength used for the pump.

Figure 5a shows the false-color map of the TA spectra obtained for the Ag@CeO$_2$ sample using a pump at 275 nm, above the band gap of CeO$_2$, and the visible probe. The map shows new TA features at delay times shorter than 10 ps (Figure 5a): a broad positive band around 610 nm, a broad negative band at 380-520 nm and a sharp positive band below 350 nm (see also Supporting Information, Figure S7). These features are assigned to the LSPR of Ag NPs, and they present the typical decay times of transient plasmonic signals (< 10-15 ps). The signals originate from the heating induced by excited electrons, which promote strong changes in the dielectric constant of the material and thus a change of the LSPR response of the NPs [53]. This change typically leads to a bleaching of the central part of the resonance and to a simultaneous increased TA intensity in the wings.[48] At delay times larger than 10 ps the map in Figure 5a presents only the positive photoinduced absorption peak, assigned to CeO$_2$ and already discussed for the bare CeO$_2$ film (Figure 4b), which persists in all the delay time range investigated, i.e. up to 500 ps. Figure 5b reports the false-color map of the TA spectra obtained for the Ag@CeO$_2$ sample with a pump at 440 nm, below the band gap of CeO$_2$, and the visible probe. The pump energy corresponds to LSPR excitation in the Ag NPs (Figure 2). Also in this case at delay times shorter than 10 ps LSPR signals are observed, similar to the ones observed in the TA map obtained with the pump at 275 nm (Figure 5a). The main point to note is that the map of the Ag@CeO$_2$ at time delays higher than 10 ps (**Errore. L'argomento parametro è sconosciuto.**b) exhibits the same persistent signal at 345 nm assigned to photoinduced absorption in CeO$_2$, although the pump energy is below the CeO$_2$ band gap. The presence of the photoinduced absorption signal is ascribed to transient occupation of 4f levels in CeO$_2$ induced by LSPR-mediated electron injection. Figure 4d clearly shows that in the CeO$_2$ sample without Ag nanoparticles the intensity at 345 nm is zero, with a pump at 440 nm, supporting the hypothesis made on the origin of the TA signal.

To obtain further information on the electron injection mechanism and on its efficiency, we compared the time evolution of the photoinduced absorption signal in the different samples, excited at the different pump energies, by considering horizontal cuts of the TA maps at 345 nm (Figure 6). The TA of the CeO$_2$ film pumped above its band gap (Figure 6a) increases very rapidly within the first 5 ps and it slowly decays at longer times. The signal was fitted using a linear combination of a rising function to describe the increase at short times and a decreasing exponential function to obtain the slow decay. Each function was convolved with the instrument response function (see Supporting Information for details). The fitting function obtained is used as a fingerprint of ceria de-excitation in the fits of the TA decay of the other samples. The photoinduced absorption signal for the Ag@CeO$_2$ sample pumped at 275 nm (Figure 6b) shows an additional LSPR-related decrease of intensity below 10 ps (the LSPR positive wing), which is described by introducing into the fit a further exponentially decreasing function with a short decay time. The signal of the Ag@CeO$_2$ sample pumped at 440 nm (Figure 6c) was fitted by a linear combination of the ceria-related and LSPR-related functions, obtaining very similar decay times (see table S1, Supporting Information). The good quality of the fit (green line in Figure 6c) is consistent with the transient occupation of the Ce 4f levels when the Ag@CeO$_2$ system is pumped below its bandgap at the Ag LSPR wavelength, and it indicates a plasmon-mediated charge transfer between the Ag NPs and the oxide. The dynamics of the electron injection at delay times shorter than 5 ps cannot be accessed, because the CeO$_2$-related signal is superimposed with the TA signal related to the LSPR of the Ag NPs (see also Supporting Information, Figure S7).

A quantification of the injection efficiency was obtained by comparing the TA signals at 345 nm of the Ag@CeO$_2$ sample pumped at different energies below the band gap, with the same signal on CeO$_2$ film pumped at 275 nm, in the 50-250 ps delay time range, i.e. after the decay of the LSPR-related transient signals. In this delay time range, the photoinduced absorption signal of CeO$_2$ dominates and its intensity is proportional to the density of electrons in the cerium oxide 4f

ha formattato: Pedice

ha formattato: Pedice

ha eliminato: Figure 4Figure 4

ha formattato: Tipo di carattere: Non Grassetto, Inglese americano, Proporzioni car 108%

ha formattato: Tipo di carattere: Non Grassetto, Inglese americano, Proporzioni car 108%

ha eliminato: Figure 5Figure 5

ha formattato: Tipo di carattere: Non Grassetto, Inglese americano, Proporzioni car 108%

ha formattato: Tipo di carattere: Non Grassetto, Inglese americano, Proporzioni car 108%

ha formattato: Evidenziato

ha eliminato: **Error! Unknown switch argument.**

ha eliminato: above (

ha eliminato:)

ha eliminato: convoluted

ha eliminato: below (

ha eliminato:)

ha eliminato: fitting function

ha eliminato: a

ha formattato: Tipo di carattere: Non Grassetto, Proporzioni car 108%

ha eliminato: Figure 6Figure 6

ha formattato: Tipo di carattere: Non Grassetto, Proporzioni car 108%

ha eliminato: the use of

ha eliminato: Figure 5Figure 5

ha formattato: Tipo di carattere: Non Grassetto, Inglese americano, Proporzioni car 108%

ha formattato: Tipo di carattere: Non Grassetto, Inglese americano, Proporzioni car 108%

ha formattato: Pedice

ha formattato: Pedice

ha formattato: Tipo di carattere: Non Grassetto, Inglese americano, Proporzioni car 108%

ha eliminato: Figure 5Figure 5

ha formattato: Tipo di carattere: Non Grassetto, Inglese americano, Proporzioni car 108%

band after the excitation. Assuming that each photon with energy higher than the bandgap excites an electron from the valence band to the Ce 4f levels, to obtain the injection efficiency we compared the number of excited electrons per

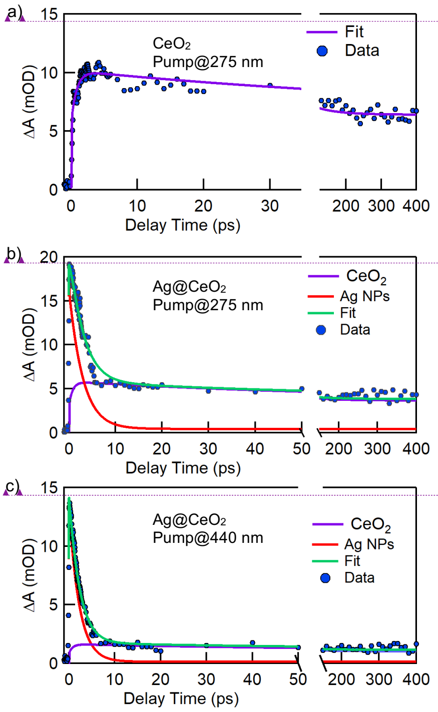

Figure 6. Time dependence of transient excited state signal at 345 nm of the CeO_2 sample pumped at 275 nm (a) and of the $Ag@CeO_2$ sample pumped at 275 nm (b) and at 440 nm (c). The components used for data fitting, related to photoinduced absorption in CeO_2 (purple line) to plasmonic deexcitation (red line), and the full fitting spectrum (green line) are also shown as solid lines.

incident photon in the $Ag@CeO_2$ sample at different pump energies below the band gap to the number obtained for the CeO_2 film with a pump above the band gap.

We estimated the incident photon density at the different pump fluences and energies with the formula:

$$\boldsymbol{n_{ph}} = \frac{\boldsymbol{A(\lambda_{pump})\cdot F}}{\boldsymbol{D\cdot \hbar\omega_{pump}}},$$

where $\boldsymbol{A(\lambda_{pump})}$ is the absorbance of the sample at the pump energy, F is the pump fluence, D is the total sample thickness and $\boldsymbol{\hbar\omega_{pump}}$ is the pump energy.[9] Then, we correlate this result with the density of electrons in the 4f levels, obtained by calculating the integral of the photoinduced absorption signal in the 50-250 ps time interval. The results for the CeO_2 film pumped at 275 nm and for the $Ag@CeO_2$ sample pumped at 440 nm are shown in Figure 7a together with their linear fits, obtained by fixing the intercept to 0 mOD·ps (see Supporting Information for further details). The slopes κ of the lines as in Figure 7a are proportional to the electron population in the 4f levels at each pump energy. The ratio between the κ values for the $Ag@CeO_2$ sample and the reference CeO_2 film gives the efficiency of the charge injection from Ag NPs to cerium oxide. The resulting injection efficiencies at the different pump energies are shown in Figure 7b. Surprisingly high values in the 12-16 % range have been obtained for excitation between 400 and 500 nm, while a lower value of 6% is found for the pump at 600 nm.

To understand such high efficiencies we first consider mechanisms such as light trapping,[18] energy transfer to the semiconductor through near-field enhancement,[19] plasmon induced radiative energy transfer,[19] and plasmon induced resonant energy transfer.[19] The similar slopes of the $Ag@CeO_2$ sample and CeO_2 film pumped at 275 nm reported in Figure 7a, indicate a similar excitation of the ceria with and without Ag NPs. This evidence suggests that the light trapping gives a negligible contribution to the injection efficiency, as expected for such small NPs.[18] All the mechanisms considered up to now require an overlap between the LSPR and an optical transition in the semiconductor and they were not expected to contribute significantly in the sample here considered.

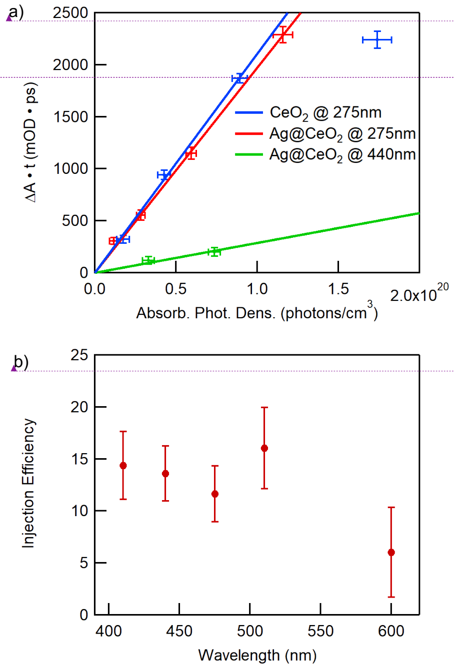

Figure 7. a) ΔA·t vs absorbed photon density and b) injection efficiency as a function of pump wavelength.

ha formattato: Tipo di carattere: Non Grassetto, Proporzioni car 108%

ha eliminato: Figure 7Figure 7

ha formattato: Tipo di carattere: Non Grassetto, Proporzioni car 108%

ha formattato: Tipo di carattere: 9 pt

ha formattato: Tipo di carattere: 8 pt

ha formattato: Tipo di carattere: Non Grassetto, Proporzioni car 108%

ha eliminato: Figure 7Figure 7

ha formattato: Tipo di carattere: Non Grassetto, Proporzioni car 108%

ha eliminato: Figure 7Figure 7

ha formattato: Tipo di carattere: Non Grassetto, Proporzioni car 108%

ha formattato: Tipo di carattere: Non Grassetto, Proporzioni car 108%

ha formattato: Tipo di carattere: 9 pt

ha formattato: Tipo di carattere: 8 pt

ha formattato: Tipo di carattere: 9 pt

ha formattato: Tipo di carattere: 9 pt

ha formattato: Tipo di carattere: 8 pt

ha formattato: Tipo di carattere: 9 pt

We therefore concentrate our discussion on the mechanisms which do not require an overlap between the LSPR of the metal NPs and an optical transition in the semiconductor, such as plasmon-induced indirect hot electron injection[2] and plasmon-induced direct electron injection.[22,54] Until recently it was thought that only the first of these mechanisms could induce an electron injection in the oxide. The dephasing and the decay of the LSPR excitation inside the NPs lead to a non-thermal energy distribution of hot electrons, followed by injection of a part of the distribution over/through the Schottky barrier formed at the interface between the metal and the semiconductor due to band bending. A large body of research in the literature is dedicated to this mechanism, spawning an entire field of research called hot carrier science.[20,55,56] Indeed, numerous systems have been identified in which this mechanism takes place. The efficiency of this process is intrinsically limited by competition with electron thermalization within the metal leading to a hot Fermi-Dirac energy distribution in which most electrons do not have sufficient energy to overcome the Schottky barrier. Furthermore, the electron initially formed must have its moment vector directed towards the interface in order to be injected into the semiconductor. White and Catchpole estimated a maximum injection efficiency of 8% for this indirect plasmonic mechanism in the case of Au@TiO_2. [57] It should be noted that Ag is known to be more efficient at generating hot electrons than Au.[58] Nonetheless the true maximum efficiency is likely to be lower than this, especially when considering the optimistic assumptions, such as a flat energy distribution of non-thermal electrons formed by LSPR decay up to the energy of the absorbed photon, employed in the above estimate. Based on these considerations, we suggest that other processes in addition to hot electron injection are at work in this system.

The plasmon-induced direct electron injection mechanism, which was theoretically proposed by Long and Prezhdo[54] to have a very high efficiency of 50% in the Au@TiO_2 system, is the instantaneous generation of charge-separated states across the metal/semiconductor interface following the dephasing of the LSPR. This prediction was confirmed by the measurement of an electron injection efficiency of 24% in the Au@CdSe system.[22] Furthermore, Tan et al. [59] experimentally demonstrated in the Au@TiO_2 system that the direct dephasing of the LSPR excitation in Au formed electrons in TiO_2 on the sub-10 fs timescale.[23] It is possible that the high efficiencies of electron injection observed in the Ag@CeO_2 system are partly due to this direct mechanism.

A further point to be discussed is how the injection efficiency varies with pump wavelength. We observe a drop in the injection efficiency at 600 nm with respect to that in the 400 - 500 nm range (see Figure 7b), even though the absorption cross section remains quite constant (see Figure 2). In the case of the indirect injection mechanism one could justify this observation if the LSPR excited at 600 nm produces fewer hot electrons with energy sufficient to overcome the barrier between the metal and the semiconductor than excitation in the 400 – 500 nm range. Based on photon energy considerations alone this is certainly possible, however it has also been observed that the efficiency of hot electron generation depends on the intensity of the hot spots of the NPs. In the system studied here, the hot spots generated for excitation of the longitudinal LSPR resonance at 580 nm are significantly more intense than those generated at the transverse resonance at 420 nm. This is evident in Figure 8, where the electric near field enhancement simulations (performed using MNPBEM toolbox[34]) of the two excitation modes are compared.

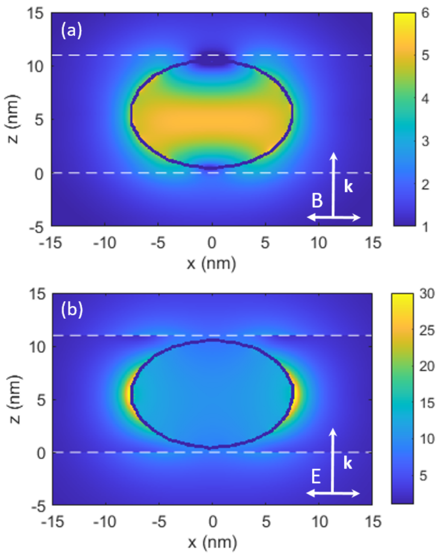

Figure 8. Field enhancement, defined as |E/E_0| (where the E_0 is the electric field of the incident radiation and E the resultant one), in ellipsoidal Ag NP with 15 nm major axis and 10 nm minor axes, embedded in 11 nm of ceria, in the case of incident radiation (a) with electric field parallel to the minor axis and energy at the LSPR along that direction (460 nm); (b) with electric field parallel to the major axis and energy at the LSPR along that direction (590 nm). The filed enhancement in the two cases is so large to prevent the possibility of using a common false color scale.

The direct injection mechanism is strongly modulated by the coupling of the density of the states in the semiconductor (the 4f levels with a narrow energy width) and the plasmonic resonances at the interface. For this reason, the resulting injection efficiency does not follow the absorption cross section of the Ag NPs. Depending on the positioning of the Fermi level of the metal within the band gap of the CeO_2, some plasmonic excitations at specific energies can be more efficient than others in injecting electrons into the Ce 4f states. However, it is difficult to make a quantitative and precise estimate of these energies due to the sensitivity of the Fermi level to the crystal structure of the NPs and the uncertainty of the position of the energy bands of the semiconductor due to interface effects.[60,61]

The observed plasmon-mediated electron injection efficiency is indeed expected to largely influence the properties of the cerium oxide surrounding the Ag NPs. The long-living charges injected in Ce 4f levels will temporarily modify the oxidation state of the corresponding Ce ions from 4+ to 3+, decreasing the energy for oxygen vacancy formation in the cation neighborhoods. If the oxide layer embedding the Ag NPs is thin enough, surface oxygen vacancies will be easily formed, thus increasing the catalytic activity of the material. This mechanism is expected to induce a sensitization of the material to visible light to promote and catalyze redox reactions.

Conclusions

We have investigated the static and transient optical properties of Ag NPs embedded within a cerium oxide matrix. The interpretation of the results is based on a detailed morphological characterization. The NPs have an icosahedral shape, a narrow size distribution centered around 10 nm, and they are partially aggregated into clusters of two or more NPs. The system shows a strong absorption band in the visible region, assigned to LSPRs, in agreement with simulations made using a boundary element method approach. Femtosecond transient absorption spectroscopy measurements show a transient occupation of the Ce 4f levels also at pump energies below the band gap of the cerium oxide. The observed phenomenon is ascribed to plasmon-mediated electron injection from Ag NPs to cerium oxide. The electron injection efficiency was quantified to be in the 6-16% range and to vary with the pump energy. The high efficiency revealed suggests that the indirect hot electron injection is not the only mechanism active in this system. We therefore suggest that a direct process, in which electrons are injected into the semiconductor by direct dephasing of the plasmonic resonances at the interface, has to be taken into account. The information obtained for the long-living plasmon-mediated charge injection discussed in this work is of great importance for a knowledge-driven design of new efficient ceria-based nanostructured photocatalytic materials.

Conflicts of interest

There are no conflicts to declare.

Acknowledgements

DC, PO'K, SDA and SV acknowledge funding from PRIN project no. 2015CL3APH.
SV and SDA acknowledge funding from Università degli Studi di Modena e Reggio Emilia through FAR2016 project titled: “Innovative (oxide-based) materials and methods for fuel cell electrodes implementation.”

Author Contributions

PL, POK, DC, SDA and SV conceived the experiment. JSPC, MCS, and SDA prepared the samples and did the XPS analysis. MCS, GB and JSPC did the TEM analysis. JSPC, SB and ADB did the UV-Vis spectrophotometry analysis. JSPC, DC, POK, LDM, AP did the FTAS experiment. POK and JSPC did the BEM simulations. All authors contributed to data interpretation and to manuscript writing.

References

1 M. J. Kale, T. Avanesian and P. Christopher, *ACS Catal.*, 2014, **4**, 116–128.

2 C. Clavero, *Nat. Photonics*, 2014, **8**, 95.

3 H. Chen and L. Wang, *Beilstein J. Nanotechnol.*, 2014, **5**, 696–710.

4 P. Narang, R. Sundararaman and H. A. Atwater, *Nanophotonics*, 2016, **5**, 96–111.

5 L. Liu, X. Zhang, L. Yang, L. Ren, D. Wang and J. Ye, *Natl. Sci. Rev.*, 2017, **4**, 761–780.

6 N. Wu, *Nanoscale*, 2018, **10**, 2679–2696.

7 Y. Zhang, S. He, W. Guo, Y. Hu, J. Huang, J. R. Mulcahy and W. D. Wei, *Chem. Rev.*, 2018, **118**, 2927–2954.

8 Z. Liu, W. Hou, P. Pavaskar, M. Aykol and S. B. Cronin, *Nano Lett.*, 2011, **11**, 1111–1116.

9 D. C. Ratchford, A. D. Dunkelberger, I. Vurgaftman, J. C. Owrutsky and P. E. Pehrsson, *Nano Lett.*, 2017, **17**, 6047–6055.

10 T. G. U. Ghobadi, A. Ghobadi, E. Ozbay and F. Karadas, *ChemPhotoChem*, 2018, **2**, 161–182.

11 A. Primo, T. Marino, A. Corma, R. Molinari and H. García, *J. Am. Chem. Soc.*, 2011, **133**, 6930–6933.

12 S. Navalon, M. de Miguel, R. Martin, M. Alvaro and H. García, *J. Am. Chem. Soc.*, 2011, **133**, 2218–2226.

13 S. M. Kim, H. Lee, K. C. Goddeti, S. H. Kim and J. Y. Park, *J. Phys. Chem. C*, 2015, **119**, 16020–16025.

14 W. Lei, T. Zhang, L. Gu, P. Liu, J. A. Rodriguez, G. Liu and M. Liu, *ACS Catal.*, 2015, **5**, 4385–4393.

15 G. N. Vayssilov, Y. Lykhach, A. Migani, T. Staudt, G. P. Petrova, N. Tsud, T. Skála, A. Bruix, F. Illas, K. C. Prince, V. Matolín, K. M. Neyman and J. Libuda, *Nat. Mater.*, 2011, **10**, 310–315.

16 N. V. Skorodumova, S. I. Simak, B. I. Lundqvist, I. A. Abrikosov and B. Johansson, *Phys. Rev. Lett.*, 2002, **89**, 166601.

17 A. Laachir, V. Perrichon, A. Badri, J. Lamotte, E. Catherine, J. C. Lavalley, J. Elfallah, L. Hilaire, F. Lenormand, E. Quemere, G. N. Sauvion and O. Touret, *J. Chem. Soc. Trans.*, 1991, **87**, 1601–1609.

18 H. A. Atwater and A. Polman, *Nat. Mater.*, 2010, **9**, 205–213.

19 X.-C. Ma, Y. Dai, L. Yu and B.-B. Huang, *Light Sci. &Amp; Appl.*, 2016, **5**, e16017.

20 P. Christopher and M. Moskovits, *Annu. Rev. Phys. Chem.*, 2017, **68**, 379–398.

21 N. Wu, *Nanoscale*, 2018, **10**, 2679–2696.

22 K. Wu, J. Chen, J. R. McBride and T. Lian, *Science*, 2015, **349**, 632–635.

23 S. Tan, A. Argondizzo, J. Ren, L. Liu, J. Zhao and H. Petek, *Nat. Photonics*, 2017, **11**, 806–812.

24 S. K. Cushing, J. Li, F. Meng, T. R. Senty, S. Suri, M. Zhi, M. Li, A. D. Bristow and N. Wu, *J. Am. Chem. Soc.*, 2012, **134**, 15033–15041.

25 X. Kong, Z. Wang and A. O. Govorov, *Adv. Opt. Mater.*, 2017, **5**, 1600594.

26 H. Harutyunyan, A. B. F. Martinson, D. Rosenmann, L. K. Khorashad, L. V Besteiro, A. O. Govorov and G. P. Wiederrecht, *Nat. Nanotechnol.*, 2015, **10**, 770–774.

ha eliminato: :

ha formattato: Tipo di carattere: Grassetto

ha eliminato: steady

ha eliminato: dynamic

ha eliminato: /1-166601/4

ha formattato: Tipo di carattere: Grassetto, Inglese americano

ha formattato: Inglese americano

ha formattato: Inglese americano

ha eliminato: *(80-.).*

27 L. V Besteiro and A. O. Govorov, *J. Phys. Chem. C*, 2016, **120**, 19329–19339.

28 J. W. Hong, D. H. Wi, S.-U. Lee and S. W. Han, *J. Am. Chem. Soc.*, 2016, **138**, 15766–15773.

29 E. Cortés, W. Xie, J. Cambiasso, A. S. Jermyn, R. Sundararaman, P. Narang, S. Schlücker and S. A. Maier, *Nat. Commun.*, 2017, **8**, 14880.

30 M. W. Knight, Y. Wang, A. S. Urban, A. Sobhani, B. Y. Zheng, P. Nordlander and N. J. Halas, *Nano Lett.*, 2013, **13**, 1687–1692.

31 C. Ng, P. Zeng, J. A. Lloyd, D. Chakraborty, A. Roberts, T. A. Smith, U. Bach, J. E. Sader, T. J. Davis and D. E. Gómez, *arXiv Prepr. arXiv1711.07095*.

32 P. Luches, F. Pagliuca, S. Valeri, F. Illas, G. Preda and G. Pacchioni, *J. Phys. Chem. C*, 2012, **116**, 1122–1132.

33 C. A. Schneider, W. S. Rasband and K. W. Eliceiri, *Nat. Methods*, 2012, **9**, 671–675.

34 U. Hohenester and A. Trügler, *Comput. Phys. Commun.*, 2012, **183**, 370–381.

35 F. J. García de Abajo and A. Howie, *Phys. Rev. B*, 2002, **65**, 115418.

36 F.-C. Chiu and C.-M. Lai, *J. Phys. D. Appl. Phys.*, 2010, **43**, 075104.

37 E. D. Palik, *Handbook of Optical Constants of Solids*, 1985.

38 F. Toschi, D. Catone, P. O'Keeffe, A. Paladini, S. Turchini, J. Dagar and T. M. Brown, *Adv. Funct. Mater.*, 2018, **28**, 1707126.

39 S. D'Addato, V. Grillo, S. Altieri, S. Frabboni, F. Rossi and S. Valeri, *J. Phys. Chem. C*, 2011, **115**, 14044–14049.

40 L. D. Marks, *Reports Prog. Phys.*, 1994, **57**, 603.

41 S. D'Addato, D. Pinotti, M. C. Spadaro, G. Paolicelli, V. Grillo, S. Valeri, L. Pasquali, L. Bergamini and S. Corni, *Beilstein J Nanotechnol*, 2015, **6**, 404–413.

42 W.-H. Kim, W. J. Maeng, M.-K. Kim, J. Gatineau and H. Kim, *J. Electrochem. Soc.*, 2011, **158**, g217.

43 S. Guo, H. Arwin, S. N. Jacobsen, K. Järrendahl and U. Helmersson, *J. Appl. Phys.*, 1995, **77**, 5369–5376.

44 B. Choudhury and A. Choudhury, *Mater. Chem. Phys.*, 2012, **131**, 666–671.

45 X. Lu, D. Zheng, P. Zhang, C. Liang, P. Liu and Y. Tong, *Chem. Commun.*, 2010, **46**, 7721.

46 P. Patsalas, S. Logothetidis, L. Sygellou and S. Kennou, *Phys. Rev. B - Condens. Matter Mater. Phys.*, 2003, **68**, 035104.

47 M. M. Khan, S. A. Ansari, D. Pradhan, D. H. Han, J. Lee and M. H. Cho, *Ind. Eng. Chem. Res.*, 2014, **52**, 9754–9763.

48 G. V. Hartland, *Phys. Chem. Chem. Phys.*, 2004, **6**, 5263.

49 H. Cha, D. Lee, J. H. Yoon and S. Yoon, *J. Colloid Interface Sci.*, 2016, **464**, 18–24.

50 L. Amidani, A. Naldoni, M. Malvestuto, M. Marelli, P. Glatzel, V. DalSanto and F. Boscherini, *Angew. Chemie*, 2015, **127**, 5503–5506.

51 P. J. Hay, R. L. Martin, J. Uddin and G. E. Scuseria, *J. Chem. Phys.*, 2006, **75**, 1–6.

52 F. Esch, S. Fabris, L. Zhou, T. Montini, C. Africh, P. Fornasiero, G. Comelli and R. Rosei, *Science (80-.).*, 2005, **309**, 752–755.

53 G. V. Hartland, *Chem. Rev.*, 2011, **111**, 3858–3887.

54 R. Long and O. V. Prezhdo, *J. Am. Chem. Soc.*, 2014, **136**, 4343–4354.

55 M. L. Brongersma, *Proc. IEEE*, 2016, **104**, 2349–2361.

56 A. Furube and S. Hashimoto, *NPG Asia Mater.*, 2017, **9**, e454.

57 T. P. White and K. R. Catchpole, *Appl. Phys. Lett.*, 2012, **101**, 073905.

58 G. V Hartland, L. V Besteiro, P. Johns and A. O. Govorov, *ACS Energy Lett.*, 2017, **2**, 1641–1653.

59 S. Tan, A. Argondizzo, J. Ren, L. Liu, J. Zhao and H. Petek, *Nat. Photonics*, 2017, **11**, 806–812.

60 R. T. Tung, *Phys. Rev. B*, 1992, **45**, 13509–13523.

61 K. Antoine, *Mater. Horizons*, 2016, **3**, 7–10.

ha formattato: Tipo di carattere: Grassetto

ha eliminato:

ha formattato: Tipo di carattere: Grassetto

ha eliminato: DOI:10.1088/0022-3727/43/7/075104